



ACOUSTICS 2012

Acoustical properties of macroscopically inhomogeneous porous medium

K. V. Horoshenkov^a, S. Masaharanon^a, K. Khan^a, A. Geslain^b, J.-P. Groby^b
and O. Dazel^b

^aUniversity of Bradford, Great Horton Road, BD7 1DP Bradford, UK

^bLaboratoire d'acoustique de l'université du Maine, Bât. IAM - UFR Sciences Avenue Olivier
Messiaen 72085 Le Mans Cedex 9
k.horoshenkov@brad.ac.uk

A 140 mm thick material sample with a distinctive pore size stratification was produced in the laboratory from polyurethane binder mixed with recycled particulates. This material exhibits a high acoustic absorption across a relatively broad range of frequencies. It was shown that the observed absorption coefficient spectra depend clearly on the sample orientation. The state vector formalism and Peano series expansion were adopted to explain the observed acoustic absorption behaviour of the developed material sample. A Biot-type model was used to link the acoustic pressure gradient with particle velocity in the oscillatory flow in the material pores. The complex dynamic density and bulk modulus of the equivalent fluid in the material pores were predicted using a computationally efficient model based on the Pade approximation. A good agreement between the proposed theory and the obtained experimental data for the acoustic absorption coefficient was observed.

1 Introduction

Porous materials are commonly used to absorb acoustic noise. These materials are typically efficient in a broad frequency range only when the acoustic wavelength (λ) is smaller or comparable to the layer thickness (L) and when there is a good match between the impedance of the surrounding fluid ($\rho_0 c$) and the surface impedance of the porous layer (z_s). As a result, the maximum absorption of a highly porous layer is typically achieved when the input resistance ($\text{Re}(z_s)$) of the acoustic is approximately equal to the input reactance ($\text{Im}(z_s)$). In this case, the optimal flow resistivity of the porous material R_b is determined by the following conflicting criteria: (i) $R_b \approx 0.34\rho_0 c/(\Omega L/\lambda)$; and (ii) $R_b k L \ll 1$, where k is the wavenumber in air and Ω is the material porosity. An obvious problem here is that the required thickness of the porous layer needs to increase proportionally with the increased wavelength to ensure that the latter condition remains satisfied. Since it is impractical to install acoustic absorbers which thickness is comparable with the acoustic wavelength, a majority of conventional porous absorbers are typically designed to perform well in the medium and high frequency regimes, i.e. at frequencies of 500 Hz and above.

In order to improve the low-frequency absorption performance of porous layers, it is common to stack a discrete number of homogeneous porous layers to reduce gradually the mismatch between the acoustic impedance of air and the input impedance of the resultant material structure. Although this technology is well established, there has been little or no experimental studies which can demonstrate that an improvement in the absorption coefficient can be obtained by producing a material with continuous pore stratification, and that the acoustical properties of this structure can be accurately modeled on the basis of a limited number of measured microstructural parameters. Therefore, purpose of this work is to fill this gap by presenting new experimental data on the acoustical and non-acoustical properties a porous material in which a continuous pore stratification has been achieved. This material is produced using a relatively simple chemical reaction process which is described in detail. The obtained experimental data are then used to validate the model for the acoustical properties of porous media with pore stratification proposed recently by De Ryck *et al* [1]. The model is based on the alternative Biot's formulation [2] in which the dynamic complex density and compressibility are given by the expression proposed in the work by Horoshenkov and Swift [3]. In this way the variation in the pore size distribution data obtained for several piecewise quasi-homogeneous sub-layers can be accounted for and used to predict the acoustic behavior of the entire material specimen. The full equations of macroscopically inhomogeneous poroelastic material were solved by use of the state vector (Stroh) formalism

together with Peano series expansion in the work by Gautier *et al*[4]. This can classify as a standard method to model wave propagation in material with anisotropy, e.g. elastic materials with stratification, and in functionally graded materials [5]. The approach can also account for continuously varying properties in poroelastic media or in porous media with rigid frame and help to avoid problems related to a coarse parameter discretization. Here, the method is derived and applied to macroscopically inhomogeneous porous materials under the rigid frame approximation.

2 Equations of macroscopically inhomogeneous porous materials under the rigid frame approximation

Rather than to deal directly with the temporal representation of the acoustic field in a porous inhomogeneous layer, $\bar{s}(\mathbf{x}, t)$ (with $\mathbf{x} = (x_1, x_2)$), we will prefer to deal with its Fourier transform, $s(\mathbf{x}, \omega)$. These representations are related by $\bar{s}(\mathbf{x}, t) = \int_{-\infty}^{\infty} s(\mathbf{x}, \omega) e^{i\omega t}$, wherein $\omega = 2\pi\nu$ is the angular frequency, with ν the frequency.

From the alternative Biot's formulation [2], the equations of motion in a macroscopically inhomogeneous porous material under the rigid frame approximation were derived in [1]. These equations take the following form

$$\begin{cases} i\omega p = \tilde{K}_{eq}(\mathbf{x}) \nabla \cdot \mathbf{V} , \\ i\omega \tilde{\rho}_{eq}(\mathbf{x}) \mathbf{V} = \nabla p , \end{cases} \quad (1)$$

where p is the fluid pressure in the material pores and \mathbf{V} is the equivalent velocity vector for the oscillatory fluid flow in the interconnected pores. Here, the porous medium can be assumed to behave as an equivalent fluid with the equivalent, frequency and space dependent fluid density, $\tilde{\rho}_{eq}$, and bulk modulus, \tilde{K}_{eq} . These quantities account for the viscous and thermal losses. Rather than to use the common Johnson-Champoux-Allard model [6, 7], the close to log-normal distribution of pore size is considered [3]. According to this model, the equivalent density and compressibility depend on the characteristics of the saturating fluid, the porosity Ω , the tortuosity q^2 , the static flow resistivity R_b , and the standard deviation in the log-normally distributed pore size, σ . These four last parameters are supposed to be space dependant. The pores are assumed of circular, cylindrical shape.

3 Numerical evaluation of the pressure field

3.1 Description of the configuration

Both the incident plane acoustic wave and the plate are assumed to be invariant with respect to the Cartesian coordinate x_3 . A cross-sectional x_1 - x_2 plane view of the 2D scattering problem is shown in Figure 1. The upper and lower

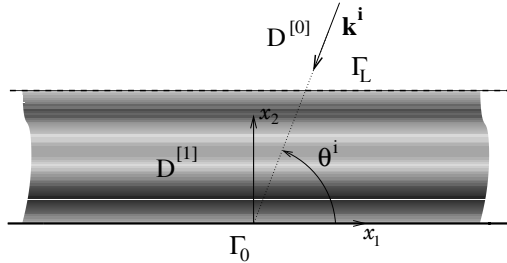


Figure 1: Cross-sectional plane view of the configuration.

boundaries of the layer are flat and parallel. They are designated by Γ_L and Γ_0 and their x_2 coordinates are L and 0 . The porous material $M^{[1]}$ occupies the domain $D^{[1]}$. The inhomogeneity (stratification) of the material layer occurs along the x_2 direction, i.e. Ω , q^2 , R_b , and σ are x_2 depth-dependent. The surrounding and saturating fluid is the air medium.

The wavevector \mathbf{k}^i of the incident plane wave lies in the sagittal plane and the angle of incidence is θ^i measured counterclockwise from the positive x_1 axis. The incident wave initially propagating in $D^{[0]}$ is expressed by $p^i(\mathbf{x}) = e^{i(k_1 x_1 - k_2^{[0]}(x_2 - L))}$, wherein $k_1 = -k^{[0]} \cos \theta^i$ and $k_2^{[0]} = k^{[0]} \sin \theta^i$. The uniqueness of the solution to the forward-scattering problem is ensured by the radiation condition

$$p^{[0]}(\mathbf{x}) - p^i(\mathbf{x}) = e^{i\mathbf{k}^{[0]} \cdot \mathbf{x}} / \sqrt{|\mathbf{x}|}; \quad |\mathbf{x}| \rightarrow \infty, \quad x_2 > L. \quad (2)$$

3.2 The state vector formalism and Peano series expansion

The spatial Fourier transform $\widehat{s}(x_2, k_1)$ of $s(\mathbf{x})$ is first introduced. This transform can be written in the form $s(\mathbf{x}, \omega) = \widehat{s}(x_2, k_1, \omega) e^{i k_1 x_1}$ because of the plane wave nature of the excitation.

After spatial Fourier transform of (1) and rearrangement, the problem also reduces to the solution of the first order differential matrix system for the column state vector $\widehat{\mathbf{W}} = \langle \widehat{p}^{[1]}, \widehat{V}_2^{[1]} \rangle$, which takes the form:

$$\frac{\partial}{\partial x_2} \widehat{\mathbf{W}} - \begin{bmatrix} 0 & i\omega \widetilde{\rho}_{eq}(x_2) \\ \frac{i\omega}{\widetilde{K}_{eq}(x_2)} \left(1 - \left(\frac{k_1}{\widetilde{k}_{eq}(x_2)} \right)^2 \right) & 0 \end{bmatrix} \cdot \widehat{\mathbf{W}} = \frac{\partial}{\partial x_2} \widehat{\mathbf{W}} - \mathbf{A} \cdot \widehat{\mathbf{W}} = \mathbf{0}, \quad (3)$$

where $\widetilde{k}_{eq}(x_2) = k^{[1]} = \omega \sqrt{\widetilde{\rho}_{eq}(x_2) / \widetilde{K}_{eq}(x_2)}$. The matrix \mathbf{A} is x_2 -dependent, because $\Omega(x_2)$, $q^2(x_2)$, $R_b(x_2)$, and $\sigma(x_2)$, are x_2 -dependent.

The solution of system (3) takes the following form

$$\widehat{\mathbf{W}}(L) = \mathbf{M} \cdot \widehat{\mathbf{W}}(0), \quad (4)$$

where \mathbf{M} is the so-called matricant[8], which relates the value of the state vector $\widehat{\mathbf{W}}(0)$, at $x_2 = 0$, to the value of the state vector $\widehat{\mathbf{W}}(L)$, at $x_2 = L$. Since \mathbf{A} is x_2 dependent and does not commute for different values of x_2 , i.e. $[\mathbf{A}(x_2), \mathbf{A}(x_2')] = \mathbf{A}(x_2)\mathbf{A}(x_2') - \mathbf{A}(x_2')\mathbf{A}(x_2) \neq 0$, $\forall (x_2, x_2') \in [0, L]^2$, $x_2 \neq x_2'$, the matricant \mathbf{M} is defined by the so-called multiplicative integral satisfying the Peano expansion[5, 9, 8, 10]. The Peano series reads as

$$\mathbf{M} = \mathbf{I} + \int_0^L \mathbf{A}(x_2) dx_2 + \int_0^L \mathbf{A}(x_2) \left(\int_0^{x_2} \mathbf{A}(\zeta) d\zeta \right) dx_2 + \dots \quad (5)$$

and its evaluation is performed via the following iterative scheme

$$\begin{cases} \mathbf{M}^{[0]} = \mathbf{I}, \\ \mathbf{M}^{[n]} = \mathbf{I} + \int_0^L \mathbf{A}(x_2) \mathbf{M}^{[n-1]}(x_2) dx_2, \end{cases} \quad (6)$$

such that $\lim_{n \rightarrow \infty} \mathbf{M}^{[n]} = \mathbf{M}$.

3.3 The boundary value problem

The application of the boundary conditions at both interfaces Γ_L (continuity of pressure $\widehat{p}^{[1]}(L) = \widehat{p}^{[0]}(L)$ and normal component of the velocity $\widehat{V}_2^{[1]}(L) = \frac{1}{\rho^{[0]}} \left. \frac{\partial \widehat{p}^{[0]}(x_2)}{\partial x_2} \right|_{x_2=L}$) and Γ_0 ($\widehat{V}_2^{[1]}(0) = 0$) yields the state vectors $\widehat{\mathbf{W}}(L)$ and $\widehat{\mathbf{W}}(0)$, which are required to solve the problem. From the separation of variables, the radiation conditions, and the spatial Fourier transform, the spatial Fourier transform of the pressure field in $D^{[0]}$ can be written as

$$\widehat{p}^{[0]} = e^{-i k_2^{[0]}(x_2 - L)} + R e^{i k_2^{[0]}(x_2 - L)}, \quad (7)$$

where R is the acoustic reflection coefficient. The state vectors become

$$\widehat{\mathbf{W}}(L) = \mathbf{S} + \mathbf{L}^L R \quad \text{and} \quad \widehat{\mathbf{W}}(0) = \mathbf{L}^0 \cdot \widehat{p}^{[1]}(0), \quad (8)$$

wherein \mathbf{S} accounts for the excitation of the system by the plane incident wave, \mathbf{L}^L relates the unknown R to the state vector $\widehat{\mathbf{W}}(L)$, and \mathbf{L}^0 relates the unknown $\widehat{p}^{[1]}(0)$ to the state vector $\widehat{\mathbf{W}}(0)$.

Finally, the introduction of (8) in (4) gives rise to the final system of equations, whose solution contain the reflection coefficient R

$$\left[\left[\mathbf{L}^L \right] \left[-\mathbf{M} \cdot \mathbf{L}^0 \right] \right] \cdot \left[\frac{R}{\widehat{p}^{[1]}(0)} \right] = -\mathbf{S}, \quad (9)$$

This system is solved for each frequency and directly provide the reflection coefficient associated with the plane incident wave. The pressure field in $D^{[0]}$ can then be calculated through $p^{[0]} = \widehat{p}^{[0]} e^{i k_1 x_1}$.

This numerical procedure was validated by comparing the results obtained by the present method to those calculated by the classical transfer matrix method provided by MAINE3A at both normal and oblique incidence for a known two-layers porous material, modeled with the usual Johnson-Champoux-Allard model [6, 7], considered as a single inhomogeneous layer.

4 Sample preparation procedure

The material sample investigated in this work was manufactured in the Acoustics Laboratory at the University of

Bradford. A composition of a polyurethane binder supplied by Chemique Adhesive (XP 2261), low molecular weight polyol supplied by Rosehill Polymers Ltd (Flexilon 1117) and tyre shred residue supplied by Credential Tyre Recycling Ltd was used in the material manufacturing process. Tyre shred residue was a mix of granulated nylon fibres and rubber particles that are bonded to the fibres as illustrated in Figure 2. A majority of the fibres and grains in tyre shred residue fell into the 0.25–5.0 mm size range. This range controlled to some extent the minimum and maximum pore dimensions that were achieved in the sample production experiment. The polyurethane polymerisation reaction was activated when water was added and the ingredients were mixed for approximately 60 seconds. This time was found to be sufficient to ensure good mixing of the ingredients in the mix and adequate level of aeration that was needed to help to initiate the polymerization reaction.

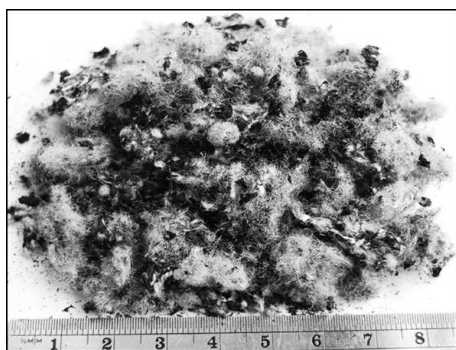


Figure 2: Tyre shred residue used in the material production process.

The resultant mixture was poured in a cylindrical mould with a terminated bottom and an open top. The diameter of this mould was 100 mm and its height 150 mm. In this way, the polymerization reaction occurred in a container with the top surface vented to the atmosphere and the bottom sealed. Oxygen in the atmosphere helped to decrease the reaction time at the surface of the material created in this mould. The reaction time here relates directly to expanding time in the foaming process. A shorter expanding time from a fast reaction of the foaming processes results in smaller pores in the top layer of the material. Carbon dioxide (CO_2) products of the slower reaction at the bottom of the mould can be trapped by the top material layers which solidify more rapidly. Therefore, a slower polymerisation reaction at the bottom of this mould has a longer expanding time resulting in larger pore sizes. It was estimated that the reaction took on average 60 min to complete resulting in a fully consolidated sample of expanded polyurethane foam with the stratified pores. After that time the porous sample was removed from the mould and its top and bottom surfaces were trimmed with to form a 140 mm long porous cylinder with smooth top and bottom surfaces. Photographs of the resultant material sample (porous cylinder) and its top and bottom surfaces are shown in Figure 3.

5 Material characterisation procedure

The acoustical and related non-acoustical properties of the material sample were measured using the following procedure. Firstly, the acoustical impedance and absorption co-

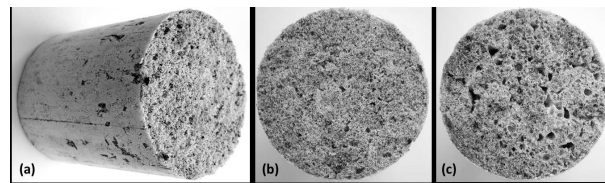


Figure 3: Photographs of the 140 mm thick material sample with pore stratification.

Table 1: The values of the four non-acoustical parameters as a function of the layer depth.

Layer depth (mm)	Ω	q^2	R_b (N.s.m ⁻⁴)	σ
140 (1)	0.757	2.236	125200	0.570
105 (1)	0.731	2.800	117600	0.633
105 (2)	0.702	1.725	64000	1.199
70 (2)	0.718	1.017	46730	1.613
70 (3)	0.738	2.245	57730	0.807
35 (3)	0.740	1.606	43780	1.183
35 (4)	0.768	1.976	29110	0.635
0 (4)	0.745	1.803	24520	0.761

efficient of the original 140 mm porous cylinder was measured in the direct and reverse orientations. This experiment was carried out in a 100 mm diameter, two-microphone Bruel & Kjael (BK4206) impedance tube at a normal angle of incidence and in the frequency range of 50 – 1600 Hz using standard procedure. The direct orientation corresponded to the case when the acoustic excitation in the impedance tube was applied to the top surface of the sample which contained smaller pores. The reverse orientation was the opposite, i.e. when the acoustic excitation was applied to the bottom surface of the material sample, i.e. to the surface that consisted of larger pores. Secondly, the porous cylinder was sliced into four sub-layers each having the thickness of 35 mm. The acoustical properties of each of these four sub-layers were measured in the impedance tube in the direct and reverse orientations to study the effect of pore stratification.

The measured acoustic absorption coefficient data for each individual sub-layer were input in a standard optimization algorithm to deduce the flow resistivity, R_b , porosity, Ω , tortuosity, q^2 , and standard deviation in the pore size, σ . An objective function was adopted to minimize the following difference

$$F(\mathbf{z}) = \sum_{n=1}^N |\alpha_{exp}(f_n) - \alpha_{th}(f_n, \mathbf{z})| \rightarrow \min, \quad (10)$$

where f_n are the frequencies in the experimentally determined acoustic absorption coefficient spectrum, $\alpha_{exp}(f_n)$ and the design variable vector is $\mathbf{z} = \{R_b, \Omega, q, \sigma\}$. The optimization algorithm was based on the Nelder-Mead direct search optimization method. This parameter inversion was carried out for $N = 750$ in the frequency range of 100 – 1600 Hz that is a standard operational range for an impedance tube with a 100 mm diameter. The non-acoustical parameters deduced from the optimisation analysis for the four porous sub-layers are presented in Table 1. Here, the depth measurement corresponds to the direction x_2 which increases towards the top of the material specimen. The index shown in brackets in column 1 in Table 1 stands for the sub-layer number.

There is a relatively small stratification within a single sub-layer so that the model captures well its acoustical be-

haviour observed in the direct and in reverse orientations. The following conclusions can be drawn from these results (Table 1). Firstly, the material porosity is relatively independent of the depth. Secondly, the flow resistivity increases considerably with the increased layer depth and the flow resistivity of the top sub-layer is approximately 5-fold higher than that at the top. Thirdly, there is a rather complex dependence of the tortuosity and standard deviation in the pore size on the layer depth. The developed material structure appears less tortuous near the middle and more tortuous near the ends. This can be explained by a larger proportion of partly closed pores near the open ends and by a more complex interconnectivity between pores of different pore sizes found in this part of the material specimen. An opposite type of the behavior is observed in the standard deviation in the pore size distribution data, which peak appears at the medium depth where the minimum tortuosity value is also observed (see Table 1). This phenomenon is difficult to interpret without accurate pore size distribution data and it deserves a more detailed investigation.

6 Numerical results

The configuration is discretized in with 1000 points and the number of iteration for the evaluation of the Peano series is fixed at 250.

Each parameters P is approximated by a fourth order polynomial function of $P(x_2) = apx_2^4 + bpx_2^3 + cpx_2^2 + dpx_2 + e$ (Lagrangian), whose coefficients, a_p , b_p , c_p , and d_p , have been obtained by matching the polynomial function with a parameter value measured at a specific depth. The parameters at the both edges of the sample are fixed at their values at the depths of 140 mm and 0 mm. At each of the three cutting depths (105 mm, 70 mm and 35 mm), two parameters values are available: one corresponds to the upper sub-layer in the reversed orientation and the other to the lower sub-layer in the direct orientation (see Table 1). The generated profile with the fourth order polynomial function is sensitive to the choice of these values. Figure 4 depicts the profiles generated when the value at cutting depth is: (i) the mean values of the upper sub-layer in the reversed orientation and of the lower sub-layer in the direct orientation, procedure C1; (ii) the value of the lower sub-layer in the direct orientation, procedure C2; and (iii) the value of the upper sub-layer in the reversed orientation, procedure C3.

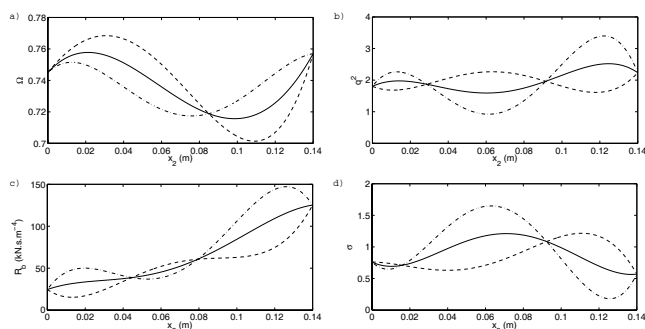


Figure 4: Profile of the parameters, a) the porosity Ω , b) the tortuosity q^2 , c) the flow resistivity R_b and d) the standard deviation in the pore size σ , when the value at each cutting depth is determined via the procedure C1 (—), the procedure C2 (---) and the procedure C3 (- · -).

Figure 5 depicts the absorption coefficient (A) calculated with the proposed theoretical model ($A = 1 - R^2$, R is the solution of system (9)) for the parameter profiles shown in Figure 4 and the measured absorption coefficients for the whole material sample. Several observations can be made on the basis of these results. Firstly, the model captures well the behavior of the measured acoustic absorption coefficient spectra throughout the considered frequency range. Secondly, the agreement between the model and the measured data is better in the case of direct sample orientation, i.e. when the sound wave is incident on the higher flow resistivity end of the sample. Thirdly, a better agreement between the modeled and measured data is obtained when the parameter values for the upper sliced sample in the reverse orientation are used (see dash-dotted lines in Figure 4). Fourthly, the largest discrepancy between the modeled and measured data is observed when the parameter values for the lower sliced sample in the direct orientation are used in the model. Fifthly, the mean parameter values enable the model to provide a sufficiently close fit (within 5%). The observed discrepancies are generally small and can be explained by the choice of the method to generate the parameter profiles shown in Figure 4. A modification of one value in the parameter profile leads to the modification of the profile as a whole and different coefficients in the Lagrangian which need to be adopted in the polynomial approximation. The values of these parameters depend to some extent on the sub-layer orientation. Clearly, there is small inhomogeneity within each of the four sub-layers and it may be necessary to refine further the material characterization procedure which was used to determine the stratification parameters shown in Table 1.

The absorption coefficient data measured for the direct and reverse sample orientations (see Figure 4) are markedly different. This points out to the fact that the sample is macroscopically inhomogeneous. The absorption coefficient spectrum measured in the reverse sample orientation (A_r) is consistently higher than that measured in the direct orientation (A_d). It is possible to illustrate with these data that the ratio of these two absorption coefficient spectra has a clear peak $\max\{A_r/A_d\} \approx 1.8$ which occurs around 220 Hz. Beyond this peak the ratio of the two spectra asymptotically approaches $A_r/A_d \rightarrow 1.2$ at 1600 Hz. This phenomenon can be mainly explained by the attained profile of the air flow resistivity, which increases gradually from $x_2 = 0$ mm to $x_2 = 140$ mm and this increase is approximately 5-fold. When the incident wave strikes at the sample which is presented in the direct orientation, the value of R_b is relatively large resulting in a poor impedance mismatch ($R_b L / \rho_0 c \approx 41$). In this case a considerable amount of the acoustic energy in the incident wave is reflected at the interface $x_2 = L$ and the spectrum of the absorption coefficient is limited. In the case, when the wave strikes at the sample presented in the reverse orientation (at $x_2 = 0$), the values of R_b is relatively small and it gradually increases with depth. There is a smaller impedance mismatch ($R_b L / \rho_0 c \approx 8$). Therefore, the strength of the reflection is smaller and the absorption coefficient is relatively large. While R_b changes considerably with depth, the stratification in the other three non-acoustical parameters, as a first approximation, is relatively small. Numerical simulations suggest that there is a little difference between the absorption coefficient spectra predicted with the actual profiles for $\Omega(x_2)$, $q(x_2)$ and $\sigma(x_2)$ as shown in Figure 4, and those predicted with their depth-averaged values. Clearly, the ef-

fect of $R_b(x_2)$ on the observed acoustic absorption coefficient spectra is dominant here. This parameter is controlled directly by the pore size distribution which changes as a function of depth. This effect seems to be well predicted by the pore size distribution model and alternative Biot's formulation approach adopted in section 2.

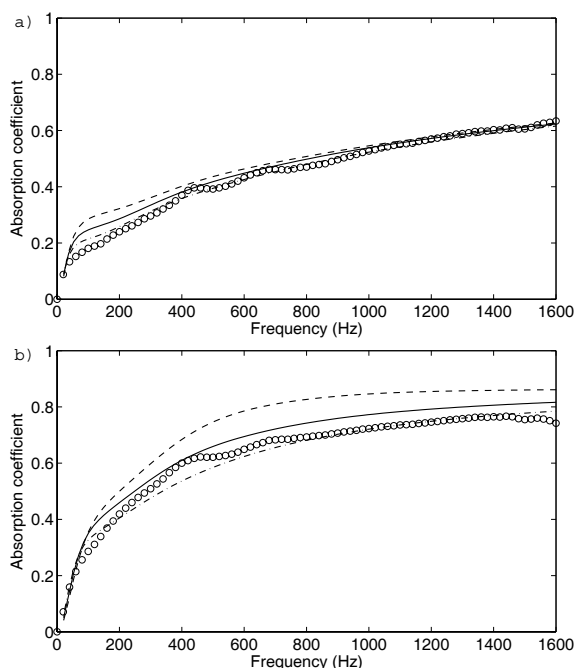


Figure 5: Absorption coefficient at normal incidence of the 140 mm thick sample in the direct and reverse orientation (o) measured and calculated when the value at each cutting depth is via the procedure C1 (—), the procedure C2 (---) and the procedure C3 (- · -).

7 Conclusions

This work presents new experimental data on the acoustic absorption coefficient of a material with continuous pore stratification. This material has been manufactured using a relative simple chemical reaction process in which a mixture of recycled grains and fibers has been bonded with a polyurethane binder. It has been shown that the reaction time is a main parameter that needs to be controlled in the foaming process in order to produce continuous pore stratification. The acoustical properties and related non-acoustical parameters of the resultant porous structure have been measured. It has been shown that the acoustical properties of this sample presented in the direct and reverse orientations are markedly different so that the developed porous structure is macroscopically inhomogeneous. The absorption coefficient spectrum measured in the reverse sample orientation is up to 80% higher than that measured in the direct orientation. This variation in the absorption coefficient spectrum is associated with the variation in the impedance mismatch when the sample orientation is reversed.

The variation in the values of the measured non-acoustical parameters have been used to explain the observed acoustic absorption coefficient spectra and their dependence on the sample orientation. It has been shown that the effect of the flow resistivity on the observed acoustic absorption coefficient spectra is dominant. This parameter undergoes an ap-

proximately 5-fold change through the 140mm sample depth. A suitable theoretical model has been adopted to explain this effect. The adopted model is based on the alternative Biot's formulation [2] and pore size distribution model proposed by Horoshenkov and Swift [3]. This model makes use of the four non-acoustical parameters: flow resistivity, porosity, tortuosity and standard deviation in the pore size which can vary as a function of sample depth. The model captures well the behavior of the measured acoustic absorption coefficient spectra throughout the considered frequency range with the accuracy of 5% or better. It has been shown that it is possible to use the parameter values which are averaged within a depth interval in which their variation is relatively small.

References

- [1] L. De Ryck, W. Lauriks, Z.E.A. Fellah, A. Wirgin, J.P. Groby, P. Leclaire, and C. Depollier. Acoustic wave propagation and internal fields in rigid frame macroscopically inhomogeneous porous media. *J. Appl. Phys.*, 102:024910, 2007.
- [2] M.A. Biot. Mechanics of deformation and acoustic propagation in porous media. *J. Appl. Phys.*, 33:1482–1498, 1962.
- [3] K.V. Horoshenkov and M.J. Swift. The acoustic properties of granular materials with pore size distribution close to log-normal. *J. Acoust. Soc. Am.*, 110:2371–2378, 2001.
- [4] G. Gautier, J.P. Groby, O. Dazel, L. Kelders, L. Deryck, and P. Leclaire. Propagation of acoustic waves in a one-dimensional macroscopically inhomogeneous poroelastic material. *J. Acoust. Soc. Am.*, 130:1390–1398, 2011.
- [5] A.L. Shuvalov, E. Le Clezio, and G. Feuillard. The state-vector formalism and the peano-series solution for modelling guided waves in functionally graded anisotropic piezoelectric plates. *Int. J. Engrg. Sci.*, 46:929–947, 2008.
- [6] J.-F. Allard and Y. Champoux. New empirical equations for sound propagation in rigid frame porous materials. *J. Acoust. Soc. Am.*, 91:3346–3353, 1992.
- [7] D.J. Johnson, J. Koplik, and R. Dashen. Theory of dynamic permeability and tortuosity in fluid-saturated porous media. *J. Fluid Mech.*, 176:379–402, 1987.
- [8] M.C. Pease. *Methods of Matrix Algebra*, chapter 6 and 7. Academic Press, New-York, 1965.
- [9] C. Baron. *Le développement en série de Peano du matricant pour l'étude de la propagation des ondes élastiques en milieux à propriétés continuellement variables*. PhD thesis, Université de Bordeaux I, 2005.
- [10] G. Peano. Intégration par série des équations différentielles linéaires. *Mathematische Annalen*, 32:450–456, 1888.